

CHANDRA OBSERVATIONS OF NGC 253: NEW INSIGHTS INTO THE NATURE OF STARBURST-DRIVEN SUPERWINDS

DAVID K. STRICKLAND AND TIMOTHY M. HECKMAN
Department of Physics and Astronomy, The Johns Hopkins University, 3400 North Charles Street, Baltimore,
MD 21218

KIMBERLY A. WEAVER
NASA/Goddard Space Flight Center, Code 662, Greenbelt, Maryland 20771

AND

MICHAEL DAHLEM
Sterrewacht Leiden, Postbus 9513, 2300 RA Leiden, The Netherlands
Accepted for publication in the Astronomical Journal

ABSTRACT

Arcsecond-resolution X-ray imaging of the nucleus of the nearby starburst galaxy NGC 253 with *Chandra* reveals a well-collimated, strongly limb-brightened, kiloparsec-scale conical outflow from the central starburst region. The outflow is very similar in morphology to the known H α outflow cone, on scales down to $\lesssim 20$ pc. This provides, for the first time, robust evidence that both X-ray and H α emission come from low volume filling factor regions of interaction between the fast energetic wind of SN-ejecta and the denser ambient interstellar medium (ISM), and not from the wind fluid itself. We provide estimates of the (observationally and theoretically important) filling factor of the X-ray emitting gas, of between ~ 4 and 40 per cent, consistent with an upper limit of ~ 40 per cent based directly on the observed limb-brightened morphology of the outflow. Only $\lesssim 20$ per cent of the observed X-ray emission can come from the volume-filling, metal-enriched, wind fluid itself. Spatially-resolved spectroscopy of the soft diffuse thermal X-ray emission reveals that the predominant source of spectral variation along the outflow cones is due to strong variation in the absorption, on scales of ~ 60 pc, there being little change in the characteristic temperature of the emission. We show that these observations are easily explained by, and fully consistent with, the standard model of a superwind driven by a starburst of NGC 253's observed power. If these results are typical of all starburst-driven winds, then we do not directly see all the energy and gas (in particular the hot metal-enriched gas) transported out of galaxies by superwinds, even in X-ray emission.

Subject headings: ISM: jets and outflows — galaxies: individual (NGC 253) — galaxies: starburst —
X-rays: galaxies

1. INTRODUCTION

Edge-on local starburst galaxies show unambiguous evidence for ~ 10 kiloparsec-scale, weakly-collimated, bipolar outflows (Heckman, Lehnert & Armus 1993). Current theory holds that these galactic superwinds are powered by the collective mechanical power of large numbers of Type II supernovae (SNe) and stellar winds, that result from the large population of massive stars formed in the starburst (Chevalier & Clegg (1985), henceforth CC). If this mechanical energy is efficiently thermalized in the starburst region (*i.e.* converted back into the thermal energy of a hot gas by shocks, as SNe and stellar winds collide), then a pressure-driven outflow from the galaxy results. The hot gas blows out of the host galaxy's ISM along the minor axis, forming the outflows seen in non-thermal radio emission, optical emission lines, and soft thermal X-ray emission in the halos of local starbursts.

Superwinds are of cosmological interest as they transport large amounts of gas, in particular newly synthesized heavy elements, and energy, into the inter-galactic medium (IGM). Quantifying this mass, metal and energy transport in local starburst galaxies is essential for understanding the significance of outflows from star-forming galaxies integrated over the history of the Universe. However, even

the basic physical properties of local superwinds such as mass outflow rates, energy content, abundances and kinematics are uncertain.

Measuring the physical properties of the hot gas driving these outflows is of crucial importance for several simple reasons. Firstly, the hot gas efficiently transports the majority of the energy of the outflow (cf. Strickland & Stevens (2000)). Secondly, the SN-heated gas is thought to contain the majority of the newly synthesized metals. Finally, this energetic gas ultimately controls the ejection of mass from the galaxy (although the majority of the mass of the outflow may be in ambient ISM swept-up by the wind, this gas is accelerated to high velocity by the hot, fast, wind fluid, cf. CC).

In principle, X-ray observations of the thermal emission from hot gas in superwinds can be used to measure the properties of the hot gas. Large amounts of *ROSAT* and *ASCA* X-ray data on starbursts already exists (see Read, Ponman & Strickland (1997); Ptak et al. (1997); Dahlem, Weaver & Heckman (1998), among others). However, the origin of the soft X-ray emission seen in local superwinds is still ambiguous. Plausible alternatives are:

1. A hot, adiabatically-expanding, volume filling fluid of stellar wind and SN-ejecta material, *i.e.* the

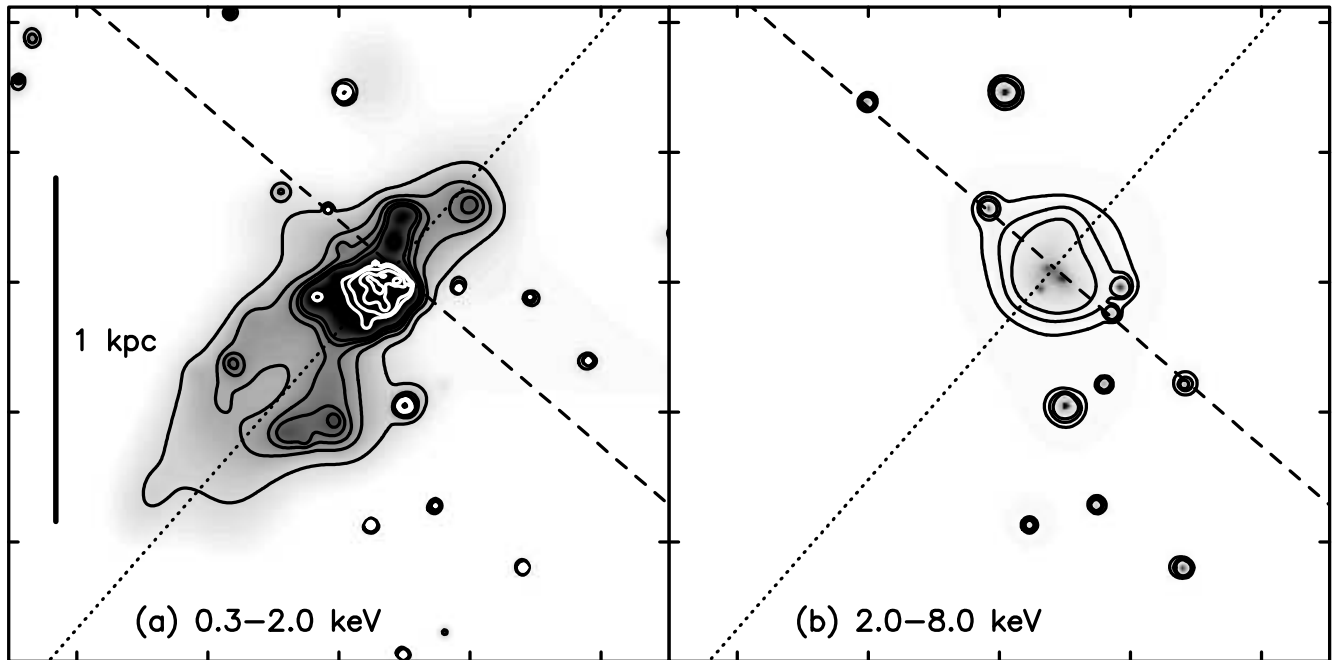


FIG. 1.— (a) *Chandra* ACIS S3 soft X-ray (0.3 – 2.0 keV) image of the center of NGC 253. Tick marks correspond to $30''$. The image, shown on a square-root intensity scale, has been adaptively smoothed and background subtracted. Contour levels shown in black start at 2.9×10^{-5} counts s^{-1} arcsec $^{-2}$, and increase in steps of 3.2×10^{-5} counts s^{-1} arcsec $^{-2}$. White contours highlight the complex high surface brightness emission within the starburst region itself, at levels of $(4.8, 6.5, 13.0, 26.0) \times 10^{-4}$ counts s^{-1} arcsec $^{-2}$. (b) The hard X-ray image (2.0 – 8.0 keV energy band) of the same region as in (a), again adaptively smoothed and shown using a square-root intensity scale. Contour levels have been chosen to highlight the clear *lack* of hard X-ray emission along the outflow lobes seen in (a). The black contour levels start at 0.7×10^{-5} counts s^{-1} arcsec $^{-2}$ (a factor 4 lower than the minimum used in (a)), and increase in multiples of two in surface brightness up to the minimum surface brightness level used in the contours of (a). In both panels the dashed and dotted lines show the position of the major and minor axes of the galaxy respectively, which intersect at the position of the brightest radio source (J2000.0, $\alpha = 00\ 47\ 33.14$, $\delta = -25\ 17\ 17.2$), which is presumed to be the nucleus (Ulvestad & Antonucci 1997).

metal-enriched, energy containing “wind” itself (e.g. Fabbiano (1988); Bregman, Schulman & Tomisaka (1995)).

2. A strongly “mass-loaded” wind, where the gas density of the hot wind has been significantly increased by efficiently mixing in cooler ambient gas (e.g. Suchkov et al. (1996)), increasing the density throughout most of the wind’s volume. Mass-loading probably occurs primarily within the starburst region.
3. Emission from low filling factor regions of interaction between the hot, high velocity, wind and clumps or clouds of ambient ISM overrun by the wind. The X-ray emitting gas in and/or around the clumps may be heated by shocks (cf. CC), by localized hydrodynamical mixing of hot wind and cooler cloud material, or by cloud evaporation due to thermal conduction.

In the first two options X-ray observations probe the wind itself, *i.e.* the gas filling the majority of the volume, containing the majority of the energy, and the majority of the metals (although heavily diluted in case 2 by ambient ISM). In the third case X-ray observations probe low filling factor material that contains little energy, mass or metal-enriched gas. It is therefore essential to know the origin of the X-ray emission, both to correctly derive the properties

of the X-ray emitting gas, and by extension those of the superwind as a whole.

In this Paper, we demonstrate the first direct observational evidence that soft thermal X-ray emission from starburst-driven superwinds arises in regions of interaction between denser ambient ISM and the hot, fast, wind fluid (case 3 above), based on *Chandra* ACIS X-ray observations of the nearby starburst galaxy NGC 253.

NGC 253 is one of the two brightest, closest¹ and best studied starburst galaxies (the other is M82). The starburst in NGC 253 has a bolometric luminosity of about $2 \times 10^{10} L_{\odot}$, and so is situated right at the “knee” of the starburst luminosity function (Soifer et al. 1987). Thus, starbursts with luminosities similar to NGC 253 dominate the starburst “emissivity” of the local universe. NGC 253 is seen almost edge-on, ideally oriented for studying the superwind as it flows out into the galaxy halo.

While both of the above attributes are shared by M82, NGC 253 offers two distinct advantages. Firstly, it lies behind a much smaller Galactic HI column than M82 (10^{20} vs. 4×10^{20} cm $^{-2}$ respectively). Since the superwind phenomenon is most conspicuous in soft X-rays, which are easily absorbed, this is a significant advantage. Secondly, NGC 253 (a late-type L_{\star} spiral) is much more typical of luminous starbursts than is M82 (a peculiar dwarf amorphous galaxy). Thus, we expect the lessons learnt from NGC 253 to be more reliably generalizable.

¹We assume the distance of $D = 2.6 \pm 0.7$ Mpc to NGC 253, given by Puche & Carignan (1988), for all calculations.

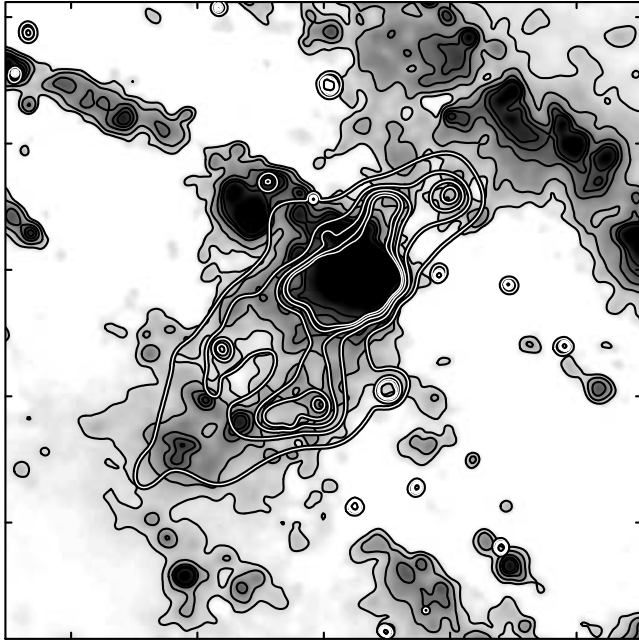


Fig. 2. — Logarithmically scaled continuum-subtracted $H\alpha$ image of the same region of NGC 253 as shown in Fig. 1. The 0.3–2.0 keV X-ray emission is shown as white contours. There is a clear similarity between the soft X-ray and $H\alpha$ emission, in particular the southern outflow cone is strongly limb-brightened in both soft X-ray and $H\alpha$ emission.

2. DATA ANALYSIS

Guest observer observations of NGC 253, using the AXAF CCD Imaging Spectrometer (ACIS²) on board the *Chandra* X-ray Observatory, were obtained on 1999 December 16, with the nuclear starburst region placed on the back-illuminated CCD chip S3.

Here we report on the soft X-ray properties of the outflow within the central kiloparsec-scale region of NGC 253, and defer further discussion, and detailed spectroscopic study, of X-ray emission from point sources and the larger-scale diffuse X-ray emission to forthcoming papers (Weaver et al. (2000); Strickland et al. (2000)).

Data reduction and analysis was performed using CIAO (v1.1.4) and HEASOFT (v5.0.1). The data were reprocessed using the latest gain correction file available at the time of writing (acisD1999-09-16gainN0003.fits), screened to remove “bad” events, and time filtered to remove periods of high background (“flares,” where the total count rate in any chip deviated by more than 5σ from the mean). This resulted in a remaining exposure length of 12862s on chip S3.

Background subtraction for both imaging and spectral analysis was performed using the background event files and software provided by the *Chandra* X-ray Center (CXC), scaled to the exposure time of our observation.

Spectra were extracted using Pulse Invariant (PI) data values, in order to account for the spatial variations in gain between different chip nodes. In order to use χ^2 as the fit statistic the spectra were rebinned to achieve a minimum of at least 10 counts per bin. Given the calibration uncertainties in the ACIS BI chip spectral response (in particular at energies below $E \sim 1$ keV), we seek only to use

spectral fitting to qualitatively characterize the emission, and do not place too much significance in the numerical results of the fits themselves.

Spectral responses were created using the latest calibration files available for observations taken with the CCD temperature of -110°C (the April 2000 release), following the example procedures provided by the CXC³. We used the spectral response appropriate for the flux-weighted center of the spatial region from which any spectrum was extracted (typically a region $\sim 40 \times 100$ raw pixels in size, see § 4). This does not fully account for the spatial variation in the ACIS spectral response, but is a good first approximation, given the current lack of publically available software to construct spectral responses for spectra from regions larger than the 32×32 pixel regions over which a single response strictly applies.

The data products initially released to us by the CXC suffered from processing errors that introduced an $\sim 9''$ shift in the absolute coordinate system for the data. For the purposes of this Paper, we registered the *Chandra* data against ground-based R-band and continuum-subtracted $H\alpha$ data, based on 9 secure optical cross-identifications of X-ray sources seen in the *Chandra* observation. This is accurate to $\sim 0.9''$ (root mean square).

3. GENERAL FEATURES OF THE X-RAY DATA

3.1. Soft X-ray emission

Many different sources of X-ray emission are visible in the *Chandra* soft X-ray (0.3 – 2.0 keV energy band) image of NGC 253 (Fig. 1a). Emerging from the nuclear starburst region, bright diffuse soft X-ray emission can be seen extending away from the plane of the galaxy to the south east and north west for a distance of ~ 1.2 and 0.6 respectively (~ 900 pc and ~ 450 pc, assuming $D = 2.6$ Mpc). This is the innermost part of the starburst-driven superwind, which has been traced with *ROSAT* out to ~ 9 kpc from the nucleus (Dahlem, Weaver & Heckman 1998). The southern lobe seen by *Chandra* is well described as a limb-brightened conical outflow, of opening angle $\theta \sim 26^\circ$, with a truncated base of diameter $\sim 24''$, similar in size to that of the starburst region itself. The outflow cone is also seen in $H\alpha$ images, and the positions and size of the X-ray and $H\alpha$ outflows match up almost exactly (see Fig. 2). Beyond a distance of ~ 600 pc from the nucleus, the X-ray emission becomes too faint to trace the limb-brightening further, and the $H\alpha$ morphology at this point becomes confused due to emission from what are known to be bright HII regions along the spiral arm seen in the background (McCarthy, Heckman & van Bruegel 1987). We analyze the spatial structure of the limb-brightened region of the southern outflow lobe in more detail in § 5.

Due to NGC 253’s inclination, the northern outflow lobe is seen through the disk of the galaxy. Strong absorption (see § 4) makes the inner region of the northern outflow less obviously conical, and it can not be traced as far as the southern outflow cone in the *Chandra* data.

Many X-ray point sources are also clearly visible, presumably high mass X-ray binaries or supernova remnants.

The peaks in the X-ray surface brightness at the south-

² *Chandra* Observatory Guide <http://asc.harvard.edu/udocs/docs/docs.html>, section “Observatory Guide”, “ACIS”

³ See the CIAO Science Threads: <http://asc.harvard.edu/ciao/threads/threads.html>

eastern-most extent of the limb-brightened region are resolved structures, and are not point-like. The effective spatial resolution of the data within the region shown in Fig. 1, measured by fitting 2-dimensional Gaussian models to the brightest point sources, is $\sim 0''.9$. As the pixel size of the ACIS instrument is $0''.492$, point sources are easily distinguished from diffuse emission in unsmoothed, unbinned, images, as most of the counts of a true point source can be found within a few adjacent pixels.

3.2. Hard X-ray emission

Hard X-ray emission from NGC 253, in the energy band 2.0 – 8.0 keV, is dominated by point source emission (see Fig. 1b). Several point-like sources are visible in the central starburst region (at least three within the central $8''$ [~ 100 pc] radius), although these are *not* the brightest X-ray sources in NGC 253.

The nucleus is surrounded by what appears to be extended hard X-ray emission, roughly spherical but somewhat elongated preferentially along the *major axis* of the galaxy, which we can trace out to a radius of $\sim 8''$ (100 pc) with confidence (in that this size is apparent to the eye in the raw, unsmoothed, data). At lower surface brightness levels the increasing apparent size and sphericity of this diffuse hard X-ray emission may be an artefact of the adaptive smoothing algorithm used. The origin and properties of this emission will be discussed in Weaver et al. (2000).

There is no significant hard X-ray emission from the the southern outflow cone, which is so clearly seen in the soft X-ray band. We shall discuss what this implies for the presence of very hot gas ($kT \geq 2$ keV) in the outflow in § 4 & 5.

4. SPECTRAL STRUCTURE WITHIN THE OUTFLOW

We shall not attempt a rigorous, quantitative, spectroscopic study of the outflow in this Paper given the uncertainties in the spectral calibration of the ACIS instrument. We believe that the data can support two *robust* conclusions:

1. The primary cause of spectral variation along, and between, the northern and southern outflow cones is due to variations in the absorption column, and not due to significant temperature variations along the outflow.
2. Features in the ACIS spectra of the diffuse emission show clear evidence for X-ray line emission from highly ionized α -elements (e.g. Mg and Si, see Fig. 3). This clearly demonstrates the thermal nature of the X-ray emission.

4.1. Simple spectral fitting

To roughly characterize the diffuse X-ray emission from the inner kiloparsec of the superwind, *i.e.* an approximate temperature and amount of foreground absorption, we divided the outflow lobes and nuclear starburst region into the set of regions shown in Fig. 3. From each region we then extracted the spectrum of the diffuse emission, having excluded any detected point sources, and used a simple one-temperature hot plasma model to fit the spectrum.

The region of the southern outflow lobe most clearly limb brightened, in both the X-ray and H α data, falls within our spectral regions S1 and S2. As this limb-brightened region is of particular interest (and is the focus of § 5), we also extracted and fitted the spectrum (Fig. 4) of this region (henceforth called the CLB region).

Only the data within the energy range between $E = 0.3$ to 3.0 keV was used in the spectral fitting, given that the 2.0 – 8.0 keV ACIS count rates for all the regions (except the starburst region NC and the northern lobe region N1) are essentially zero (see Table 1). The lack of hard X-ray emission in the southern outflow lobe is graphically demonstrated in Figs. 1 & 4.

To begin with, we fitted a variable abundance, single temperature MEKAL hot plasma model to the combined spectra from the southern outflow cone, (regions S1, S2 & S3 in Fig. 3) where a hardness ratio analysis (see § 4.2) already indicated low absorbing columns and similar spectral shape. The abundance ratios (with respect to the Solar value) of the α -elements were constrained to be equal to each other, while the abundance ratios of the other elements were forced to be equal to that of Iron.

TABLE 1
SPECTRAL FITS TO DIFFUSE X-RAY EMISSION REGIONS

Region	Count rate ^a		N_{H}^b	kT^b	$\chi^2/\text{d.o.f}$
	0.3–2.0 keV	2.0–8.0 keV	10^{20} cm^{-2}	keV	
N1	4.81 ± 0.20	0.64 ± 0.16	$92.2^{+16.6}_{-15.9}$	$0.59^{+0.12}_{-0.09}$	77.5 / 49
NC	7.67 ± 0.24	1.08 ± 0.17	$47.3^{+11.6}_{-11.8}$	$0.66^{+0.10}_{-0.08}$	128.5 / 67
S1	7.68 ± 0.25	0.15 ± 0.16	$5.6^{+3.0}_{-2.2}$	$0.63^{+0.05}_{-0.06}$	42.8 / 57
S2	5.74 ± 0.22	0.07 ± 0.16	≤ 3.4	$0.51^{+0.07}_{-0.06}$	53.1 / 45
S3	2.52 ± 0.15	0.05 ± 0.16	≤ 5.0	$0.46^{+0.13}_{-0.10}$	37.8 / 22
CLB	7.00 ± 0.20	0.09 ± 0.16	$2.1^{+2.1}_{-1.3}$	$0.57^{+0.06}_{-0.06}$	50.7 / 53

^a Background-subtracted ACIS S3 count rates in units of $10^{-2} \text{ count s}^{-1}$.

^b Confidence regions are 90% confidence for three free parameters ($\Delta\chi^2 = 6.25$).

TABLE 2
HARDNESS RATIOS IN REGION OF CLEAR LIMB BRIGHTENING

Region	PA ^a deg	Count rates ^b		Q^c
		0.3 – 1.0 keV	1.1 – 2.0 keV	
Entire CLB	130–160	6.06 ± 0.22	0.87 ± 0.09	-0.75 ± 0.04
East limb	130–137	1.58 ± 0.11	0.21 ± 0.07	-0.77 ± 0.09
Center	137–144	0.72 ± 0.08	0.10 ± 0.06	-0.76 ± 0.16
West limb	144–160	3.65 ± 0.17	0.55 ± 0.07	-0.74 ± 0.06

^a Range of position angle in the azimuthal region (see Fig. 6).

^b Background-subtracted ACIS S3 count rates in units of $10^{-2} \text{ count s}^{-1}$.

^c Hardness ratio $Q = (H - S)/(H + S)$, where H is the count rate in the 1.1 – 2.0 keV band, and S is the count rate in the 0.3 – 1.1 keV band.

This spectral fit, although of a region of very low and relatively uniform hydrogen column density (to minimize possible spectral complexity), gives strongly sub-solar abundance ratios ($Z_{\alpha} \sim 0.30^{+0.14}_{-0.10} Z_{\odot}$, $Z_{\text{Fe}} \sim 0.13^{+0.04}_{-0.03} Z_{\odot}$, 90% confidence in one interesting parameter). This is

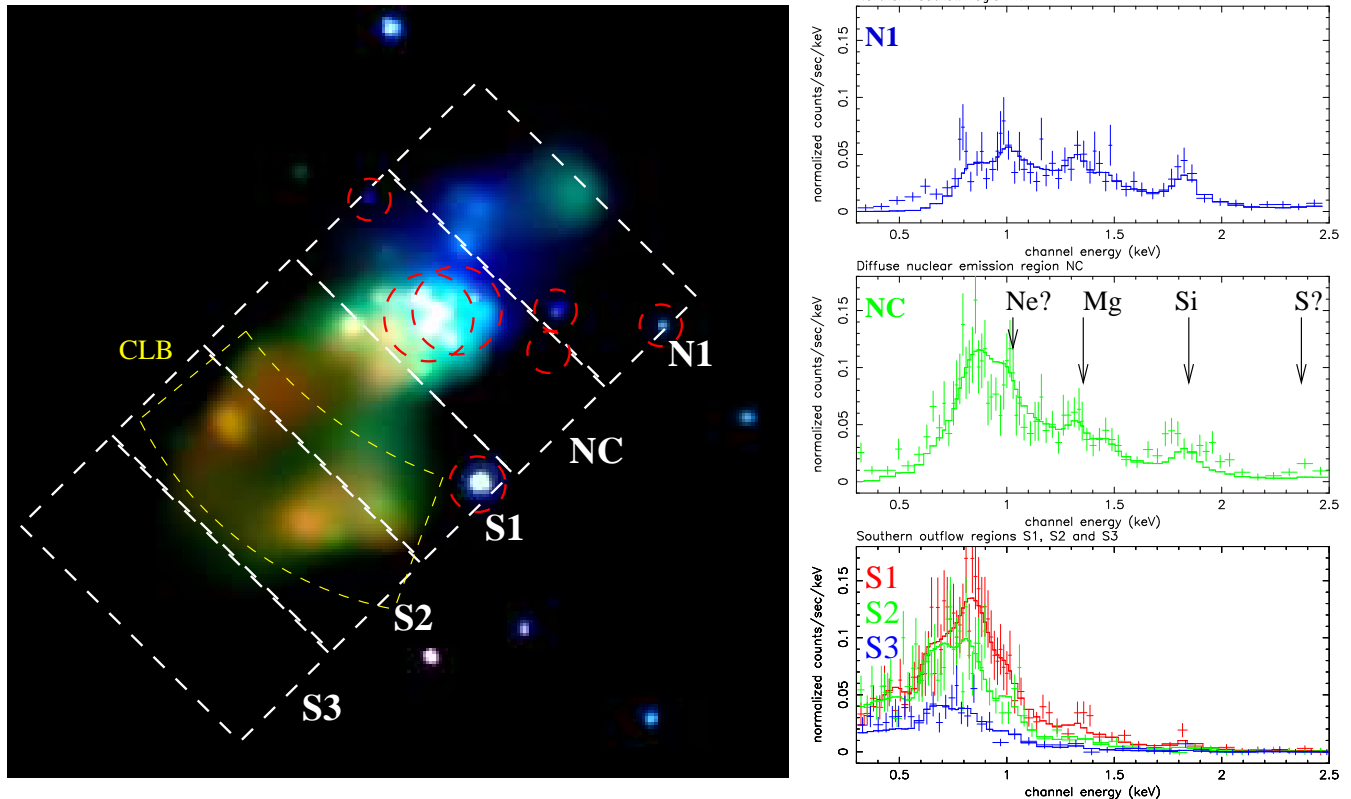


FIG. 3.— Three color, logarithmically-scaled, soft X-ray image of the central $2' \times 2'$ ($\sim 1.5 \times 1.5 \text{ kpc}^2$) region, showing the spectral variation along the outflow lobes. Emission between $0.3 \leq E(\text{keV}) < 0.6$ is shown in red, emission between $0.6 \leq E(\text{keV}) < 1.1$ in green, and emission between $1.1 \leq E(\text{keV}) < 2.0$ in blue. The south-eastern outflow cone, on the near side of the disk, becomes progressively “soft” as it rises above the absorbing H I gas in NGC 253’s disk and starburst region. In contrast, only the highest energy X-ray photons from the north-western lobe of the outflow make it through the disk without absorption. The white dashed boxes show regions from which spectra of the diffuse emission, shown in the panels on the right, were extracted. The yellow dashed line outlines the region most clearly limb brightened in both X-ray and H α images. Dashed red circles show regions of emission from point sources that were excluded in extracting the diffuse spectra. The spectra of the nuclear region and the northern outflow clearly show significant absorption at photon energies $E < 1 \text{ keV}$.

likely to be a combination of further spectral complexity on small scales (emission from multi-phase gas, cf. Strickland & Stevens (2000) and Weaver, Heckman & Dahlem (2000)) and complications arising from the uncertain and spatially varying instrument response (e.g. we believe the failure of the model to fit the spectrum of region NC in the energy range $1.6 - 2.0 \text{ keV}$ to be due to problems in the spectral response used), rather than true evidence of low metal abundances in the gas.

This spectral model was used as a template fit to all the separate regions along the outflow lobes (see Fig. 3), allowing only absorption column density, gas temperature and absolute model normalization to vary (see Table. 1). Best fit hydrogen columns vary by a factor ~ 45 , from $N_{\text{H}} \approx (9 \pm 1) \times 10^{21} \text{ cm}^{-2}$ (Northern region N1) to $N_{\text{H}} \approx 2 \times 10^{20} \text{ cm}^{-2}$ (Southern region CLB). In contrast characteristic temperatures vary by less than a factor of 2, from $kT \approx 0.66_{-0.08}^{+0.10} \text{ keV}$ (NC) to $kT \approx 0.46_{-0.10}^{+0.11} \text{ keV}$ (S3).

4.2. Hardness map

To fully exploit *Chandra*’s spectral-imaging capabilities we constructed the “hardness map,” shown in Fig. 3, of the central ~ 1.5 kiloparsec square region of NGC 253. This is a three color image of the data between (approximately) $0.3 - 0.6 \text{ keV}$, $0.6 - 1.1 \text{ keV}$ and $1.1 - 2.0 \text{ keV}$ in energy.

The southern outflow cone is clearly much softer (a higher flux of low energy X-ray photons) than the diffuse emission from the starburst region, which itself is softer than the emission seen from the northern outflow on the far side of the disk, consistent with the simple spectral fitting discussed above.

These three energy bands were chosen based on the observed spectral shape of the diffuse emission spectra. Emission in the $0.3 - 0.6 \text{ keV}$ energy band, relatively prominent in the S1 to S3 and CLB regions, is the first to be absorbed away as the foreground absorption column increases. The relative prominence of the $0.6 - 1.1 \text{ keV}$ hump (which contains the unresolved Fe L shell complex of lines) in the nuclear region (region NC) is largely due to the higher column in this region having removed much of the emission below $E = 0.6 \text{ keV}$. In region N1 the column is high enough to absorb away much of emission between $0.6 - 1.1 \text{ keV}$, making the $1.1 - 2.0 \text{ keV}$ energy band appear much stronger (and hence the spectrum harder) than in the other spectra. As the spectral fits in Table 1 show, the variation in spectral hardness of the diffuse emission is mainly due to increasing absorption.

Note that the nucleus of the galaxy lies near the north western edge of region NC (compare Figs 1 & 3), so that region N1 partially covers the most obscured part of the starburst region as well as the innermost part of the north-

ern outflow lobe.

The measured in-flight spectral resolution of the ACIS-S3 chip is ~ 0.12 keV (full width at half maximum), at the operating temperature of -110 °C that applied to these observations (see the *Chandra* Observatory Guide). The three energy bands used in Fig. 3 are therefore largely independent of each other (as can be seen from the spectra), *i.e.* “cross-talk” between the bands is minimal.

These *Chandra* observations show that emission from the wind is spectrally complex, due to spatial variations in absorption over scales as small as $\sim 5''$ (~ 60 pc), possibly with multiple temperature components on even smaller scales. The southern outflow cone is relatively spectrally uniform, having risen above the location of absorbing gas in NGC 253’s disk. Without *high spatial resolution*, X-ray spectroscopy of diffuse X-ray emission in star-forming galaxies will continue to yield ambiguous results due to mixing regions of different temperature and/or absorbing column together, in addition to problems due to blending unrelated point sources into the spectra.

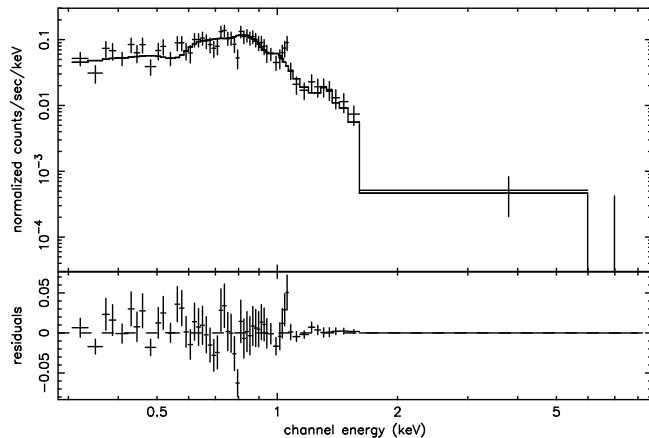


Fig. 4. — *Chandra* ACIS S3 chip X-ray spectrum of the limb brightened region of the southern outflow lobe (region CLB), fitted with a single temperature MEKAL hot plasma model. Note the lack of any additional hard X-ray component at energies above 2 keV. See § 4.1 and Table 1 for details of the spectral fit.

5. SPATIAL STRUCTURE OF THE OUTFLOW

The striking similarity between X-ray and H α emission in the southern outflow cone can be used to constrain the origin of the soft X-ray emission seen in the superwind, and its physical properties. Although it had been known from even early *Einstein* X-ray observations that the general spatial extent and distribution of X-ray-emitting gas in NGC 253 and M82 was similar to the H α emission (Watson, Stanger & Griffiths (1984); Fabbiano (1988)) the $\sim 5''$ spatial resolution, the 3 – 5'' positional uncertainties, and limited sensitivity, of both *Einstein* & *ROSAT* High Resolution Imagers (HRIs) only implied that X-ray and H α emission were similar over scales $\gtrsim 60 - 100$ pc. In contrast, our *Chandra* observations can be used to investigate the X-ray / H α correlation down to the effective resolution of the data ($\sim 0'.9 \approx 11$ pc).

5.1. Azimuthal surface brightness profiles

We looked at both azimuthal surface brightness profiles of the limb-brightened region, and at surface brightness

“slices” constructed perpendicular to the minor axis of the galaxy. Both methods give similar results, but azimuthal profiles have the advantage of preserving the conical, diverging, structure of the outflow. We use the degree of limb-brightening to constrain the fraction of X-ray and H α emission that arises in the shell or wall of the outflow, compared to emission from within the central core of the outflow itself.

We created azimuthal profiles of background-subtracted X-ray and H α surface brightness, from the region of clear limb-brightening (see Fig. 5), using 1.0° and 0.5° azimuthal bins respectively, taking care to exclude regions of emission from unrelated point sources. The resulting surface brightness profiles are shown in Fig. 6.

Both X-ray and H α azimuthal profiles peak at the same position angle on the western limb of the outflow. In both cases the eastern limb of the outflow cone is ~ 0.75 the intensity of the western limb, and the surface brightness decreases inwards of the eastern limb to a minimum value of $\sim 0.3 - 0.4$ of the peak brightness (although the X-ray peak is slightly offset to the interior of the cone from the H α). There is not such a clear decrease in brightness inwards of the western limb, but the images (Fig. 5) show additional “clouds” apparently within the outflow in both X-ray and H α images. These features might even be unrelated emission associated with the underlying disk, rather than part of the outflow itself.

We use a simple model to quantify the fraction of emission coming from within the core of the outflow, and what fraction comes from the apparent shell. We assume a conical outflow, with a uniform emissivity core I_{core} of opening angle θ_{core} , surrounded by a shell of emissivity I_{shell} and outer opening angle θ_{shell} (see Fig. 5). Predicted azimuthal profiles are convolved with Gaussian mask, to take account for the effective spatial resolution of the X-ray and H α data (FWHM = $0'.9 \equiv 0.6^\circ$ in position angle in the azimuthal profiles] for the X-ray and $1'.5$ for the H α data), and compared by eye with the data. We primarily attempt to match the position, width and intensity of the eastern limb, given the more confused state of the western side of the profiles. The relative intensity of the eastern limb with respect to the central surface brightness minimum then constrains the emissivity of any material within the core of the outflow. The best fit-by-eye shell models are shown in Fig. 6. Attempting to better match the intensity of the western limb would increase the peak-to-core intensity contrast and lead to lower values of $I_{\text{core}}/I_{\text{shell}}$.

Both the X-ray and the H α data are consistent with a hollow ($I_{\text{core}}/I_{\text{shell}} = 0$) conical outflow with $\theta_{\text{shell}} = 26^\circ$ and $\theta_{\text{core}} = 20^\circ$. The maximum value of $I_{\text{core}}/I_{\text{shell}}$ consistent with the data is ~ 0.2 (X-ray) or ~ 0.1 (H α). Both the X-ray and H α emission must therefore arise predominantly in a thin boundary layer, between a faster and/or hot tenuous wind of SN-ejecta (that invisibly fills the core of the outflow), and dense cool ambient ISM surrounding the walls of the cavity.

We looked for spectral variation between the center and walls of the southern outflow cone, in an effort to detect hotter gas from within the cone, but found no statistically significant differences. We divided the limb brightened region into three sectors, corresponding to the eastern limb, the low surface brightness core, and the western

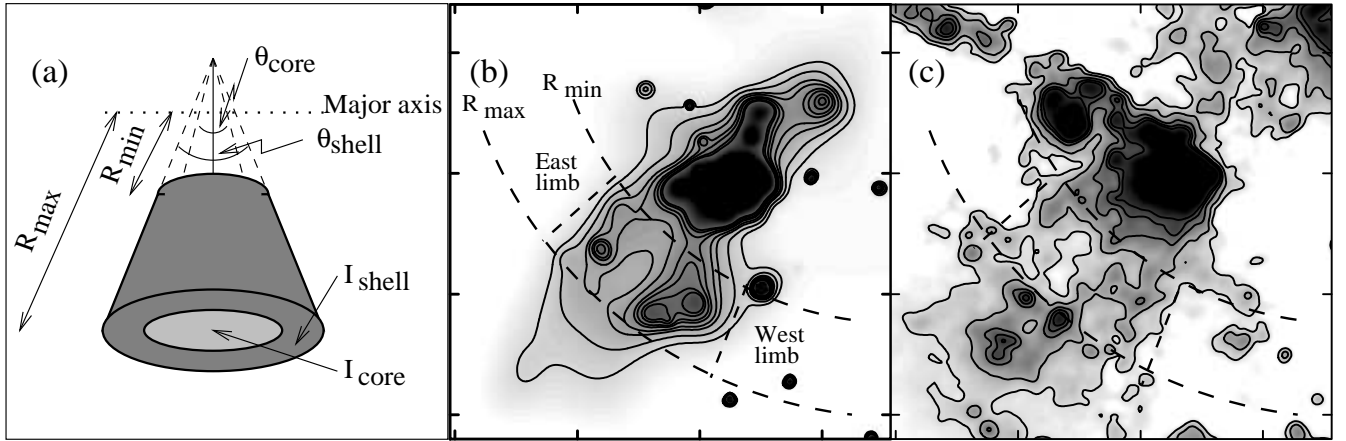


FIG. 5.— (a) Spatial model assumed for the origin of the X-ray and $H\alpha$ emission. (b) *Chandra* 0.3 – 2.0 keV image, with the region of clear limb-brightening between R_{\min} and R_{\max} , used in extracting the azimuthal surface brightness profile, shown by the curved dashed lines. This region lies between $27''$ and $47''$ ($\sim 340 - 590$ pc) from the major axis of NGC 253. These lines, along with the dashed lines parallel to the outflow, delimit the spatial region used to calculate gas masses, densities and filling factors as described in § 5. (c) As (b), but showing the same region on the $H\alpha$ image.

limb, based on the azimuthal profile shown in Fig. 6. As there were too few counts in these sub-regions for spectral fitting we constructed a hardness ratio Q from the background subtracted count rates in the two energy bands 0.3 – 1.1 keV and 1.1 – 2.0 keV, and calculated Q for the entire limb brightened region, as well as the three sub-regions (see Table. 2). Simulations with XSPEC had shown this choice of energy bands to be reasonably sensitive to changes in spectral hardness for thermal emission with temperature $kT \sim 0.1$ to 3.0 keV and hydrogen columns of between a few $\times 10^{20}$ to a few $\times 10^{21}$ cm^{-2} . This hardness ratio is more sensitive to temperature variation than using a simple ratio of 0.3 – 2.0 keV versus 2.0 – 8.0 keV count rates, for example. Both the limbs and core of the limb brightened region have hardness ratios statistically indistinguishable from one another or from the region as a whole. This is consistent with the majority of the emission, even within the projected center of the outflow cone, being from the bright walls of the cavity. Nevertheless, the uncertainty in the hardness ratio of the core region is large enough to correspond to an uncertainty in temperature (from the nominal $kT \sim 0.6$ keV) of approximately a factor two.

The spectral uniformity of the southern outflow cone allows us to interpret variations in surface brightness directly as variations in emission integral ($EI = \int n_e n_H dV$). Attempting to explain the central surface-brightness decrement of $\sim 50 - 60\%$, with respect to the apparent walls of the cone, as being purely due to absorption would require an order-of-magnitude increase in absorption column in front of the center of the cone. This would also make the surprising degree of similarity between the $H\alpha$ and X-ray azimuthal profiles an astounding coincidence, which seems unlikely. For example, assuming emission from a hot plasma with parameters equal to the best-fit model for the CLB region (see Table. 1) for the “walls” of the cavity, then reducing the flux in the center of the cone to 40% of its original value by extra absorption requires increasing the column by a factor 12 to $N_H \sim 2.5 \times 10^{21}$ cm^{-2} . This would lead to a strong decrement in the ratio of 0.3 – 0.6 keV to 0.6 – 1.1 keV count rates in the center of the cone,

relative to the walls of the cone, which is not seen. Constructing a hardness ratio from these two energy bands, in a manner analogous to those shown in Table 2, gives a hardness ratio of 0.30 ± 0.12 for the center of the cone, compared to a value of 0.35 ± 0.04 for the entire CLB region and the predicted value of 0.73 for $N_H = 2.5 \times 10^{21}$ cm^{-2} .

The inferred opening angle of the outflow, $\theta \sim 26^\circ$, is very similar to the $\theta \sim 30^\circ$ opening angle for the outflow in M82. The inferred diameter of base of the outflow, *i.e.* in the starburst region, is $\sim 24''$ (300 pc) which agrees very well with the $\sim 20''$ diameter region over which young SNRs are seen in radio observations (Ulvestad & Antonucci 1997), consistent with the idea of a SN-driven outflow.

5.2. Derived physical properties of the outflow

The maximum volume filling factor of the X-ray & $H\alpha$ emitting material in the outflow cone is then $\eta \sim 0.4$, based on the assumed geometry. If both X-ray & $H\alpha$ -emitting gas arise in a shocked or conductively heated boundary layer, in close proximity to each other, then their pressures should be similar on *local scales* (*i.e.* \lesssim a few 100 pc. On larger scales the outflow is driven by the over-pressure of the starburst region compared to the ambient ISM or IGM). We can then infer the true density of the X-ray emitting gas and its filling factor. In a 30° -wide azimuthal region centered on the position angle of the outflow cone and between the radii defined in Fig. 5, the emission integral $EI \approx 5.5 \times 10^{60}$ cm^{-3} . This is based on the observed 0.3 – 2.0 keV *Chandra* ACIS-S count rate of 0.070 ± 0.002 counts s^{-1} in this region, and assuming for simplicity emission from a $kT = 0.5$ keV hot plasma of Solar abundance, absorbed only by the Galactic foreground hydrogen column of $N_H = 10^{20}$ cm^{-2} . The total volume (*i.e.* shell + core) of the conical frustum defined by our assumed geometry is $V = 1.4 \times 10^{63}$ cm^3 , which then gives $n_e \approx 6.2 \times 10^{-2} \eta^{-1/2}$ cm^{-3} . From McCarthy, Heckman & van Bruegel (1987), $P_{H\alpha}/k \sim 1$ to 4×10^6 K cm^{-3} in the $H\alpha$ emitting gas, in the region between 250 and 500 pc from the nucleus. The true density and volume filling factor of the X-ray-emitting gas is then $n_e \sim 0.1$ to 0.3 cm^{-3}

and $\eta \sim 40$ to 4 per cent (equivalently ~ 100 to 10 per cent of the geometrical volume of the shell).

The main uncertainty affecting the derived EI is the assumed metal abundance. As we believe the fitted metal abundance to be unrealistically low, for the reasons given in § 4.1, we prefer to assume a plausible model for the emission instead of relying too heavily on simplistic spectral fits. Assuming the gas temperature is $kT \sim 0.6$ keV instead of 0.5 keV only alters the EI by ~ 0.5 per cent.

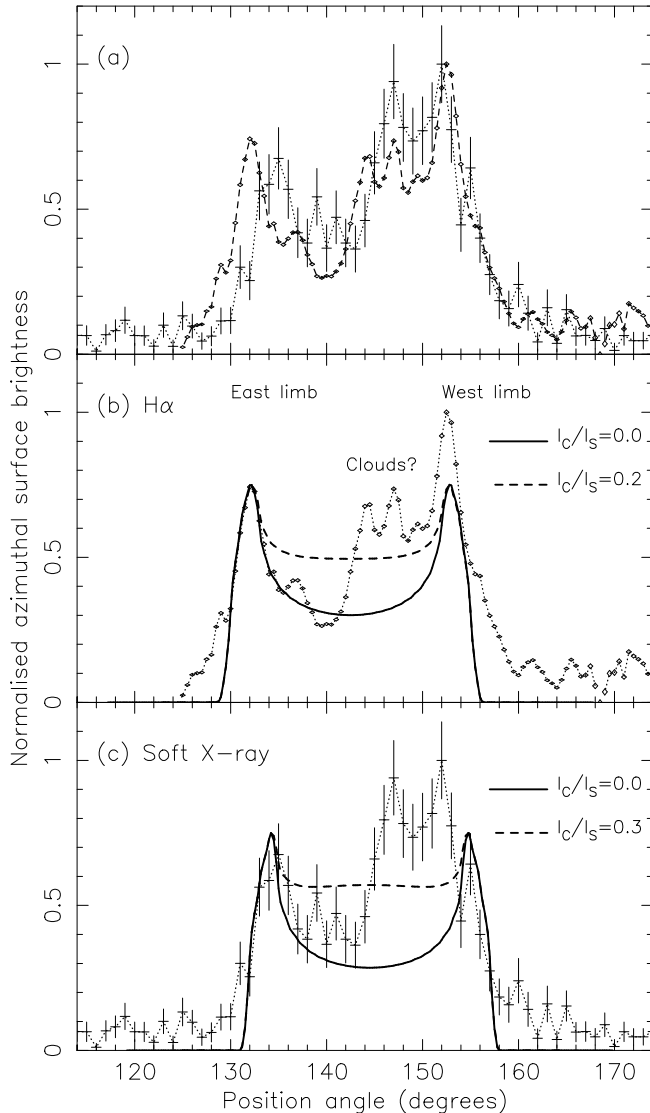


Fig. 6. — (a) Normalized azimuthal surface brightness profiles of the southern outflow cone, in H α emission (diamonds, dashed line) and 0.3 – 2.0 keV X-ray emission (crosses, dotted line). (b) H α profile, with best-fit hollow cone model ($I_{\text{core}}/I_{\text{shell}} = 0$) overlaid (solid line). A model with $I_{\text{core}}/I_{\text{shell}} = 0.2$ (dashed line) over-predicts the central surface brightness between position angles 134 – 142°. (c) As (b), but for the soft X-ray emission. Models with $I_{\text{core}}/I_{\text{shell}} \geq 0.3$ (dashed line) fail to fit the data between position angles 134 – 142°.

The total mass in X-ray emitting gas, within this specific region, is $M_{\text{X-ray}} \sim 1.5 - 6 \times 10^4 M_{\odot}$. We used the spectroscopic observations of Keel (1984) to flux calibrate our H α image (assuming a constant H α /[Ni] ratio), and hence calculate the H α flux and gas mass in the same conical frustum as used in the X-ray analysis. Assuming the

temperature of the H α emitting gas is $T_{\text{H}\alpha} = 10^4$ K, and that the electron number density of this gas is in the range $n_e = 100 - 25 \text{ cm}^{-3}$ (based on McCarthy, Heckman & van Bruegel (1987)), the mass of the H α emitting gas in this region is very similar to the mass of X-ray emitting gas, $M_{\text{H}\alpha} \sim 1 - 5 \times 10^4 M_{\odot}$. X-ray and H α gas masses are similar, despite the large difference in gas density, as the derived filling factor of the H α emitting gas within this region is substantially smaller than the filling factor of the X-ray gas ($\eta_{\text{H}\alpha} \sim 0.4 - 7 \times 10^{-4}$).

Low X-ray filling factors are a prediction of current hydrodynamical models of superwinds. In a parameter study of superwind models (Strickland & Stevens 2000), based roughly on M82’s superwind, the *globally-averaged* filling factor of the X-ray emitting gas in the *ROSAT* 0.1 – 2.4 keV energy band (roughly equivalent to the 0.3 – 2.0 keV ACIS-S energy band we have used) was always $\lesssim 2$ per cent.

Is it possible to have a wind powerful enough to compress the ambient ISM to pressures $P/k \geq 10^6 \text{ K cm}^{-3}$, yet also tenuous enough to be largely invisible in X-ray emission? In short, the answer is yes!

The maximum emission integral of X-ray-emitting gas *not* from the shell, based on $I_{\text{core}}/I_{\text{shell}} = 0.2$, is $EI_{\text{core}} = 1.2 \times 10^{60} \text{ cm}^{-3}$ ($kT = 0.5$ keV) or $3.7 \times 10^{60} \text{ cm}^{-3}$ ($kT = 2.0$ keV, a realistic value for the wind fluid temperature in this region based on the CC model). These numbers correspond to ~ 0.015 ACIS S3 count s^{-1} in the 0.3 – 2.0 keV energy band, and imply count rates in the hard 2.0 – 8.0 keV energy band of $\sim 3 \times 10^{-4}$ (assuming $kT = 0.5$ keV) or 1.6×10^{-3} count s^{-1} ($kT = 2.0$ keV). The total observed 2.0 – 8.0 keV count rate in this region is only $(0.9 \pm 1.6) \times 10^{-3}$ count s^{-1} , which can be accounted for purely by the $kT = 0.6$ keV emission from the shell (extrapolation from the 0.3 – 2.0 keV count rate predicts a 2.0 – 8.0 keV count rate of $\sim 1.4 \times 10^{-3}$ count s^{-1}). This, and the hardness ratios given in Table 2, do not rule out a spectrally harder core component to the X-ray emission in the limb brightened region, given the poor statistics. Nevertheless they suggest that the upper limits on the core emission integrals given above are conservative.

In the CC model of a freely-expanding wind, ram pressure dominates over thermal pressure at distances beyond a few starburst-region radii. For our model to work we require a wind ram pressure such that $P_{\text{ram}} = \rho_w v_w^2 \geq P_{\text{X-ray}} \sim P_{\text{H}\alpha}$, as it is the wind that shocks and compresses the ambient ISM. This is a lower limit — the wind ram pressure P_{ram} can be several times $P_{\text{H}\alpha}$ as the H α emitting material is also being swept-up and accelerated to velocities of several hundred kilometers per second by the wind. Taking this into account, let us assume $P_{\text{ram}} = \psi P_{\text{H}\alpha}$. Inspection of our existing hydrodynamical simulations of superwinds shows $1 \leq \psi \leq 10$, there being a large scatter in ψ from region to region within the wind. The *lower limit* on the emission integral of the wind fluid, required to give acceptable wind ram pressures in the same region as the limb-brightened H α and X-ray emission, is $EI_w \gtrsim V(1 - \eta_{\text{X-ray}} - \eta_{\text{H}\alpha}) \times (\psi P_{\text{H}\alpha} / 2\mu m_H v_w^2)^2 \sim 1 - 13 \times 10^{57} \psi^2 v_3^{-4} \text{ cm}^{-3}$, where v_3 is the wind velocity in units of 3000 km s^{-1} ($v_3 \sim 1$ for standard mass and energy injection rates, e.g. see Leitherer & Heckman (1995)), and assuming $\psi = 1$ to give a lower limit. Assuming that

$\psi = 3$ is typical of the wind on average, then the wind velocity must be $v_3 \geq 0.3 - 0.6$, in order not to violate the observed upper limits on wind emission integral (using the lower, and more conservative, of the two values given in the previous paragraph), which seems entirely reasonable.

These limits also make sense in terms of mass transport rates in the wind. The observed SN rate of $\sim 0.05 \text{ yr}^{-1}$ (Colina & Pérez-Olea 1992) corresponds to an expected $\dot{M}_w \sim 0.5 M_\odot \text{ yr}^{-1}$, using the Leitherer & Heckman (1995) models, and assuming no additional mass-loading. Based on the pressure balance argument, the total mass loss rate (assuming two identical outflow cones) in the wind fluid alone is $\dot{M}_w \gtrsim 0.032 - 0.13 \psi v_3^{-1} M_\odot \text{ yr}^{-1}$. The observational upper limit on the emission integral of the core of the outflow gives $\dot{M}_w < 2.2 v_3 M_\odot \text{ yr}^{-1}$, using the higher of the two EI_{core} estimates.

It is interesting to note that a clear detection of the wind component would have placed strong constraints on wind density, velocity, energetics and mass outflow rate. Separating the faint X-ray emission due to the wind from the brighter X-ray emission from wind/ISM interfaces in local starburst galaxies requires arcsecond spatial resolution — a job only *Chandra* can do.

5.3. Additional discussion

How robust are these conclusions on the origin and filling factor of the X-ray emitting gas, given the limited size of the region of unambiguous limb-brightening, the simplicity of the spatial model assumed and the uncertain value of the gas emission integral?

Although these factors probably make the estimated densities and filling factors of the X-ray emitting gas uncertain to an order of magnitude or so, the general picture of the X-ray and $\text{H}\alpha$ emission being dominated by moderate-to-low filling factor gas, arising in the interaction between the wind and denser ambient ISM, is likely to remain true. The simple analytical arguments presented in § 5.2 certainly demonstrate that our conclusions are physically plausible.

Within the region we have considered, the filling factor of the gas that is the dominant X-ray emitter *must* be less than unity, as it is impossible for a volume-filling gas to reproduce the observed limb-brightening without invoking fortuitous absorption along the center of the outflow cone. Such additional absorption would be detectable in the spectra and hardness maps, and is therefore inconsistent with the observed spectral uniformity of the southern outflow cone.

That strong limb-brightening is only observed in a narrow range of heights above the plane of the galaxy is not surprising. Within the immediate vicinity of the starburst region $\text{H}\alpha$ and X-ray emission not directly associated with the superwind itself will hide any limb-brightened outflow component. At much larger distances, as the surface brightness of the superwind decreases, limb-brightening would become increasingly difficult to detect. A well defined cavity or chimney structure with dense walls might only exist within a few scale heights of the disk. Further out in the wind, the dense gas in the outflow probably exists as isolated dense clumps and clouds dragged out of the disk (as seen in hydrodynamical simulations, e.g. Strickland & Stevens (2000)). These dense clouds, although of

low filling factor and again dominating the X-ray and optical emission, would not necessarily give a limb-brightened optical or X-ray morphology.

In principle, the filling factor of the X-ray emitting gas might be different in other parts of the flow. If density inhomogeneities in the flow are destroyed over a time scale less than or equal to the flow time, then the X-ray emission in the outer parts of the wind might be dominated by a homogenized volume-filling hot component of the wind. Detecting filamentary or “clumpy” X-ray emission at lower surface brightness in the outer parts of the wind (with *XMM-Newton* or *Chandra*) would disprove this hypothesis. However, even if the X-ray emission appears relatively uniform the filling factor is not necessarily high. It is easy to conceive of situations where low filling factor clouds dominate the X-ray emission but whose spatial distribution is so uniform as to appear smooth.

It is only with the spatial resolution *Chandra* provides that it is possible to resolve (both spectrally and spatially) the inner outflow cones (within a few hundred parsecs of the starburst region) where unambiguous evidence of the origin of the soft X-ray emission in superwinds can be found.

6. SUMMARY

Chandra ACIS observations demonstrate that the soft X-ray emission in the less-obscured of NGC 253’s superwind’s nuclear outflow cones is well collimated, and extremely similar in morphology and extent to the previously observed limb-brightened $\text{H}\alpha$ outflow cone. This provides the first direct observational evidence that both X-ray and $\text{H}\alpha$ emission come from low volume filling factor gas, regions of interaction between a tenuous starburst-driven wind of SN-ejecta and the dense ambient ISM, and not from the wind itself.

We measure the observationally and theoretically important filling factor of the X-ray emitting gas at between $\eta \sim 4$ and 40 per cent. The observed morphology of the outflow also provides a purely geometrical upper limit of $\eta \sim 40$ per cent. Only $\lesssim 20$ per cent of the observed X-ray emission can come from the volume-filling, metal-enriched, wind fluid itself. Spatially-resolved spectroscopy of the soft diffuse thermal X-ray emission reveals that the predominant source of spectral variation along the outflow cones is due to strong variation in the absorption on scales of ~ 60 pc, with little evidence for any change in the characteristic temperature of the emission. These observations are easily explained by, and fully consistent with, the standard model of a superwind driven by a starburst of NGC 253’s observed properties.

The important implication of this work is that we can not see the majority the energy and gas (in particular the hot metal-enriched gas) transported out of NGC 253 by it’s superwind, even in X-ray emission. If this is generally true for all starbursts, the majority of IGM heating and enrichment by starbursts may be currently invisible in *emission*. This emphasizes the need for, and importance of, absorption line studies of warm and hot gas in these fascinating and important objects.

We would like to thank the anonymous referee for their constructive criticism. The team that built and operates *Chandra* also deserves recognition, for their hard work,

and for making such an excellent telescope. This work was supported by NASA through grants LTSA NAG56400 and GOO-1008X.

REFERENCES

- Bregman, J.N., Schulman, E. & Tomisaka, K. 1995, *ApJ*, 439, 155
 Chevalier, R.A. & Clegg, A.W. 1985, *Nature*, 317, 44 (CC)
 Colina, L., & Pérez-Olea, D. 1992, *MNRAS*, 259, 709
 Dahlem, M., Weaver, K.A. & Heckman, T.M. 1998, *ApJS*, 118, 401
 Fabbiano, G. 1988, *ApJ*, 330, 672
 Heckman, T.M., Lehnert, M.D. & Armus, L. 1993, in "The Environment and Evolution of Galaxies," Eds. J. M. Shull and H. A. Thronson Jr, (Dordrecht:Kluwer), 455
 Keel, W.C. 1984, *ApJ*, 282, 75
 Leitherer, C. & Heckman, T.M. 1995, *ApJS*, 96, 9
 McCarthy, P.J., Heckman, T.M. & van Breugel, W. 1987, *AJ*, 92, 264
 Ptak, A., Serlemitsos, P., Yaqoob, T., Mushotzky, R. & Tsuru, T. 1997, *AJ*, 113, 1286
 Puche, D. & Carignan, C., 1988, *AJ*, 95, 1025
 Read, A.M., Ponman, T.J. & Strickland, D.K. 1997, *MNRAS*, 286, 626
 Soifer, B.T., Sanders, D.B., Madore, B.F., Neugebauer, G., Danielson, G.E., Elias, J.H., Lonsdale, C.J. & Rice, W.L. 1987, *ApJ*, 320, 238
 Strickland, D.K. & Stevens, I.R. 2000, *MNRAS*, 314, 511
 Strickland, D.K., Heckman, T.M., Weaver, K.A. & Dahlem, M. 2000, in preparation
 Suchkov, A.A., Berman, V.G., Heckman, T.M. & Balsara, D.S. 1996, *ApJ*, 463, 528
 Ulvestad, J.S. & Antonucci, R.R.J 1997, *ApJ*, 488, 621
 Watson, M.G., Stanger, V. & Griffiths, R.E. 1984, *ApJ*, 286, 144
 Weaver, K.A., Heckman, T.M. & Dahlem, M. 2000, *ApJ*, 534, 684
 Weaver, K.A., Heckman, T.M., Strickland, D.K. & Dahlem, M. 2000, in preparation